

Cobalt Borate Complex With Tetrahedrally Coordinated Co^{2+} -Promotes Lithium Superoxide Formation in Li-O_2 Batteries

Shivaraju G. Chandrappa,* Katrin Forster-Tonigold, Vasantha A. Gangadharappa, Pavithra Kannan, Kunkanadu R Prakasha, Axel Groß, Maximilian Fichtner, Rachel A. Caruso, Guruprakash Karkera, and Annigere S Prakash*

The development of non-aqueous lithium-oxygen (Li-O_2) batteries is hindered by inefficient discharge product decomposition, side reactions with the electrolyte, and high charge overpotentials (>1 V). This study explores the use of sodium cobalt borate ($\text{Na}_3\text{CoB}_5\text{O}_{10}$, NCBO) with cobalt in tetrahedral geometry as an oxygen electrocatalyst for non-aqueous Li-O_2 batteries. The prepared cobalt borate exhibits an oxygen evolution reaction (OER) overpotential of 326 mV_{RHE} at a current density of 10 mA cm^{-2} and a Tafel slope of 42 mV dec^{-1} in 1 M KOH . Density Functional Theory (DFT) calculations identify the OH-covered (101) surface of NCBO as the preferred OER site, with an overpotential between 451 and 544 mV. In Li-O_2 batteries, the NCBO cathode demonstrates 200 cycles with an overpotential of 1.95 V and 56.00% round-trip efficiency at a capacity limit of 500 mA h g^{-1} , along with a smaller charge overpotential of 0.64 V at a capacity limit of 2000 mA h g^{-1} . Post-cycling analysis of NCBO electrodes reveals electronically conductive Lithium Superoxide (LiO_2) as the dominant discharge product. As revealed by DFT studies, the promising performance of NCBO in Li-O_2 batteries is attributed to its tetrahedral Co coordination, highlighting its potential for electrocatalytic applications.

1. Introduction

Research on rechargeable Li-O_2 batteries is presently being pursued due to their high theoretical specific energy density ($\approx 3458 \text{ Wh kg}^{-1}$), which is far beyond that of conventional Li-ion batteries.^[1] However, Li-O_2 batteries are still far from being commercialized because of a range of limitations, such as poor cyclability, low power density, low-rate capability, and large charge/discharge overpotentials. These are mainly attributed to the sluggish reaction kinetics of the O_2 cathode during the lithium peroxide (Li_2O_2) formation ($2\text{Li}^+ + \text{O}_2 \rightarrow \text{Li}_2\text{O}_2$, oxygen reduction reaction, ORR) and the Li_2O_2 decomposition ($\text{Li}_2\text{O}_2 \rightarrow 2\text{Li}^+ + \text{O}_2$, oxygen evolution reaction, OER).^[2,3] The limited solubility and insulating nature of the Li_2O_2 discharge products that are deposited on the air cathode, gradually block the available

S. G. Chandrappa, V. A. Gangadharappa, P. Kannan, K. R. Prakasha, A. S Prakash
CSIR – Central Electrochemical Research Institute-Chennai Unit
CSIR Madras Complex, Taramani
Chennai, Tamil Nadu 600113, India
E-mail: shivaraju.chandrappa@upr.edu; prakash@cecri.res.in
S. G. Chandrappa, V. A. Gangadharappa, P. Kannan, K. R. Prakasha, A. S Prakash
Academy of Scientific and Innovative Research (AcSIR)
Ghaziabad 201002, India
S. G. Chandrappa, R. A. Caruso
Applied Chemistry and Environmental Science
School of Science
RMIT University
Melbourne, Victoria 3000, Australia

S. G. Chandrappa, K. Forster-Tonigold, A. Gro, M. Fichtner, G. Karkera
Helmholtz Institute Ulm for Electrochemical Energy Storage (HIU)
89081 Ulm, Germany
K. Forster-Tonigold, M. Fichtner
Institute of Nanotechnology
Karlsruhe Institute of Technology (KIT)
P.O. Box 3640, 76021 Karlsruhe, Germany
K. Forster-Tonigold, A. Gro
Institute of Theoretical Chemistry
Ulm University
89081 Ulm, Germany
S. G. Chandrappa, M. Fichtner
Institute of Inorganic Chemistry II
Ulm University
89081 Ulm, Germany



The ORCID identification number(s) for the author(s) of this article can be found under <https://doi.org/10.1002/smll.202502150>

© 2025 The Author(s). Small published by Wiley-VCH GmbH. This is an open access article under the terms of the [Creative Commons Attribution License](#), which permits use, distribution and reproduction in any medium, provided the original work is properly cited.

DOI: 10.1002/smll.202502150

surface area, resulting in poor electrochemical performance.^[4–6] Thus, continuous efforts to construct new O₂ cathode materials with improved electrochemical properties are needed to overcome these problems.

A new family of transition metal-based pentaborates Na₃MB₅O₁₀ (where M = Co, Ni, Fe, etc.) has been explored for application as a Na-ion battery cathode material by Tarascon's group.^[7] The transition metal borates offer positive attributes in structural stability, especially in oxygen co-ordination of borate over conventional oxides, and can adopt different structural orientations like diborates [B₂O₅]^{4–}, triborates [B₃O₆]^{3–}, and pentaborates [B₅O₁₀]^{5–}.^[7] In addition, conventional cobalt (Co) based oxides have high symmetry octahedral co-ordination, whereas Co based compounds containing polyanion groups (borate, phosphate, sulphate, etc.) have low symmetry co-ordination, which includes the tetrahedral (T_d), trigonal planar, and trigonal bipyramidal crystal structure. Moreover, the presence of adaptable coordination of borate groups can potentially stabilize the intermediate state of metal active sites by changing their local crystal structure with ease, thus ensuring an efficient redox change in the transition metal.^[7–9]

Recently, Baby et al.^[10] designed Zn-substituted cobalt phosphates for use as O₂ cathode catalysts in Zn-air batteries, showing the ZnCoP₂O₇ catalyst to have enhanced Zn-air battery performance compared with conventional Co-based oxides. The authors attributed the enhanced activity to the presence of asymmetric CoO₅/CoO₆ polyhedra and edge-sharing between CoO₆ octahedra and PO₄^{3–}. This allows the easy adsorption of the incoming O₂/OH[–] species on Co sites, thereby enhancing catalytic activity. Sharma et al.^[11] investigated fluorophosphate (Na₂CoPO₄F) as the O₂ cathode catalyst for aqueous Na-air battery application. The presence of F in the structure modified the Co–O bond leading to higher catalytic activity. Kim et al.^[9] reported a series of cobalt polyphosphates for OER applications. They found that Na₂CoP₂O₇ with low symmetry T_d geometry had excellent catalytic activity and stability that was comparable to conventional cobalt oxides. Dwibedi et al.^[12] reported aluandite NaCoFe₂(PO₄)₃ as a bi-functional catalyst, demonstrating that the inclusion of the phosphate group was attributed to the unique lattice structure geometry, facilitating the catalytic activity.

Solid Li₂O₂, with its electronically insulating nature, leads to higher overpotentials and adversely affects the long-term cycling stability of Li–O₂ batteries.^[13,14] In contrast, LiO₂, formed via a one-electron transfer process, exhibits higher electronic conductivity and lower charge transfer resistance, thereby contributing to a reduced charge overpotential.^[15,16] Therefore, recent research efforts have focused on developing suitable cathode catalysts that promote the dominant formation of LiO₂ as the discharge product. However, to date, mainly iridium (Ir)-based catalysts have demonstrated the ability to facilitate LiO₂ formation effectively.^[15–20]

In this study, we investigated a transition-metal polyborate-based compound for OER and as an electrocatalyst in rechargeable Li–O₂ batteries. To the best of our knowledge, transition-metal polyborates have not yet been explored as O₂ cathode catalysts for Li–O₂ batteries. This work studies the tetrahedrally coordinated Co²⁺ cobalt borate (NCBO) as the O₂ catalyst in a Li–O₂ battery. Post-cycling analysis of the NCBO electrodes revealed

that electronically conductive LiO₂ is the dominant discharge product.

2. Results and Discussion

The NCBO material was prepared by reacting sodium carbonate (Na₂CO₃), cobalt(II) hydroxide (Co(OH)₂), and boric acid (H₃BO₃) in stoichiometric amounts under continuous inert Ar gas flow at 700 °C.

Figure 1a shows the Rietveld refinement of the powder x-ray diffraction (XRD) pattern of NCBO with a goodness of fit, X² = 2.93. The XRD pattern of the NCBO can be indexed to a monoclinic structure with the space group *P*2₁/*n* and lattice parameters: *a* = 6.6448(7) Å, *b* = 18.2061(2) Å, *c* = 7.8091(8) Å, *α* = *γ* = 90°, *β* = 114.81°. The corresponding structural parameters determined by Rietveld refinement are listed in Table S1 (Supporting Information).

All atoms in the prepared borate compound are placed in general positions 4e with one crystallographic site for cobalt, three for sodium, five for boron, and ten for oxygen. The final refined atomic positions are given in Table S1 (Supporting Information). These results are in good agreement with other reported tetrahedral Co²⁺ coordinated compounds.^[7] The corresponding crystal structure of NCBO is shown in Figure 1b.

To estimate the oxidation state of elements in the prepared NCBO, X-ray photoelectron spectroscopy (XPS) studies were carried out. The survey spectrum reveals the coexistence of Na, Co, B, and O elements in NCBO (Figure S1a, Supporting Information). As can be seen in Figure 1c, the Co 2p_{3/2} and Co 2p_{1/2} doublet in the Co 2p spectrum with binding energy values of 779.80 and 796.80 eV, respectively, correlate to the presence of Co²⁺ in NCBO.^[21] The profile fitting of B 1s (Figure 1d) shows two peaks at ≈188 and ≈191 eV, which confirm the presence of B–Co and B–O bonds.^[21] The O 1s spectrum shows a peak at ≈531.7 eV, indicating the presence of the O–B bond^[22] (Figure S1b, Supporting Information).

The morphology and crystal structure of NCBO was examined on the nanoscale by transmission electron microscopy (TEM) (Figure 2). The particles appeared agglomerated and in the size range of 50–200 nm, Figure 2a,b. The selected area electron diffraction (SAED) ring pattern (Figure 2c) confirms the polycrystalline nature of the NCBO. The SAED rings were indexed to the (043) and (–371) crystal planes of the NCBO crystal structure, corresponding to d-spacings of 0.20 and 0.16 nm, supporting the XRD findings. Furthermore, energy-dispersive X-ray spectroscopy (EDX) analysis in scanning transmission electron microscopy (STEM) mode (Figure 2d–h) confirms the homogeneous distribution of Na, Co, B, and O elements throughout the as-synthesized powder.

The electrocatalytic activity of the borate compound toward oxygen evolution was investigated with linear sweep voltammetry (LSV) studies in N₂ saturated 1 M KOH electrolyte at a scan rate of 5 mV s^{–1} and 1600 rpm. As shown in Figure 3a, NCBO has an overpotential of 326 mV_{RHE} and is comparable to the commercial RuO₂ catalyst with an overpotential of 318 mV_{RHE} at an OER current density of 10 mA cm^{–2}. To acquire more information on the kinetics of OER, the Tafel plots of NCBO and RuO₂ catalysts are shown in Figure 3b, giving slopes of 42 and 82 mV dec^{–1}, respectively, indicating faster OER kinetics of the borate catalyst. More

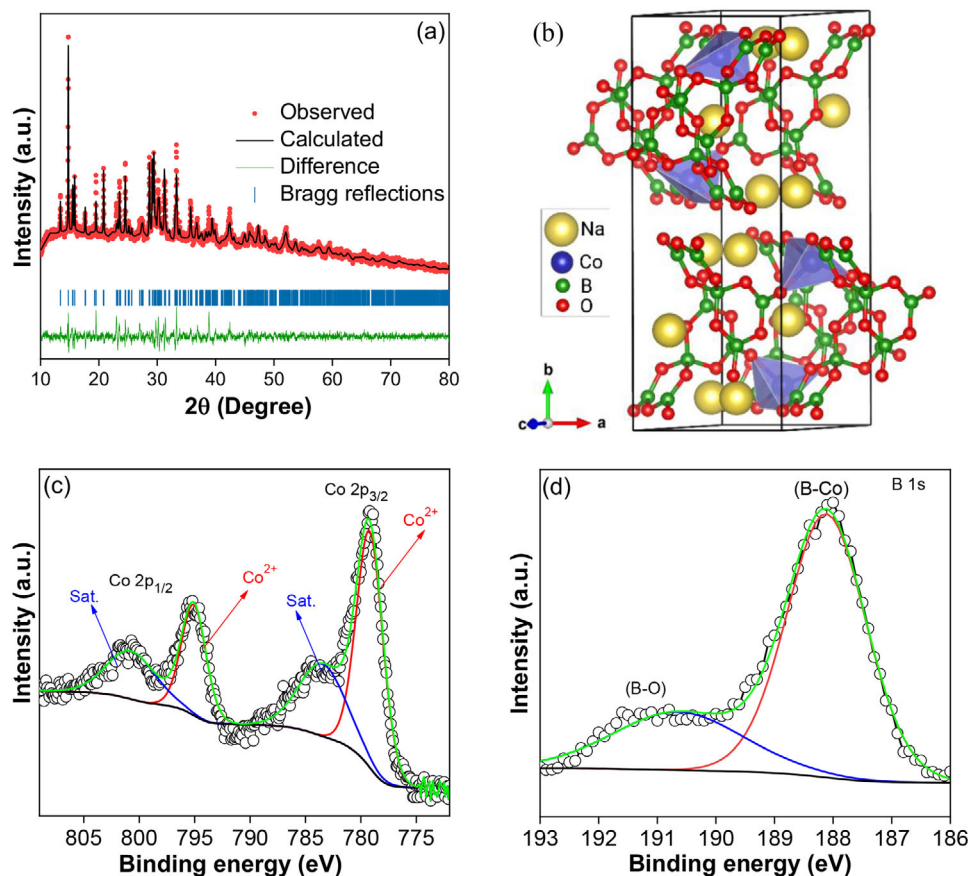


Figure 1. a) Rietveld refinement of the XRD pattern of NCBO showing the experimental data points (red), calculated pattern (black continuous line), their differences (green line), and Bragg reflections (blue tick bars). b) Crystal structure of NCBO and high-resolution XPS spectra of c) Co 2p and d) B 1s for NCBO.

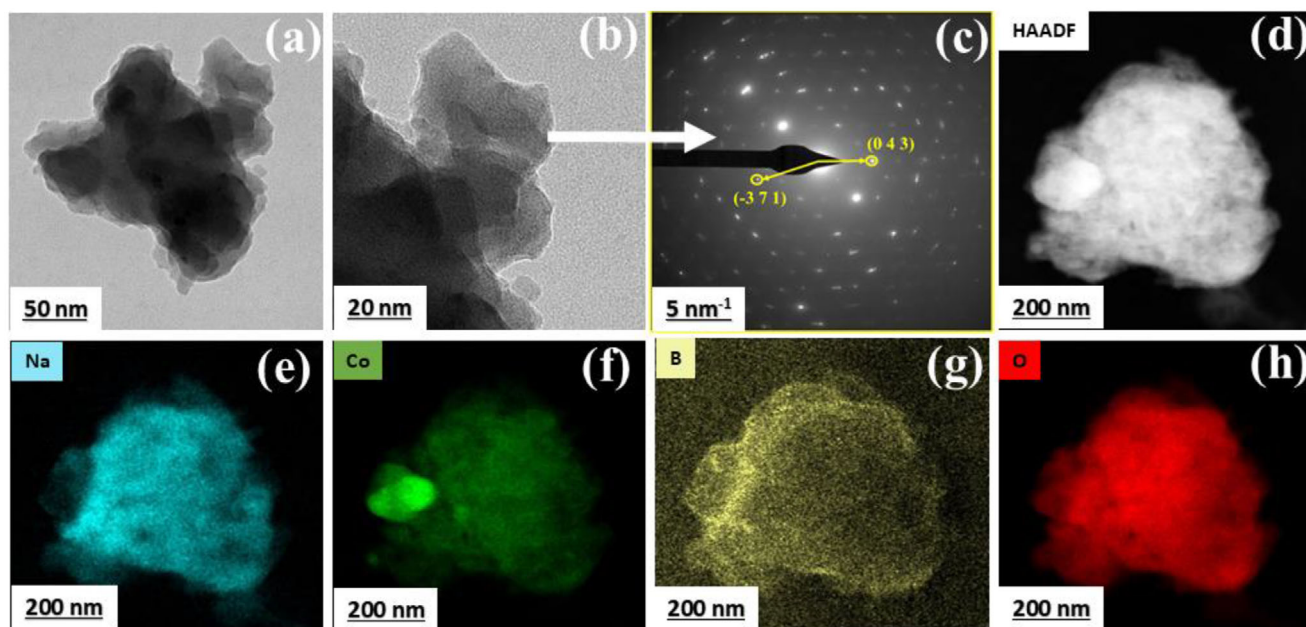


Figure 2. a, b) TEM images and c) SAED pattern of NCBO. d) High-angle annular dark-field (HAADF) image and STEM-EDX elemental mapping of e) Na, f) Co, g) B, and h) O in NCBO.

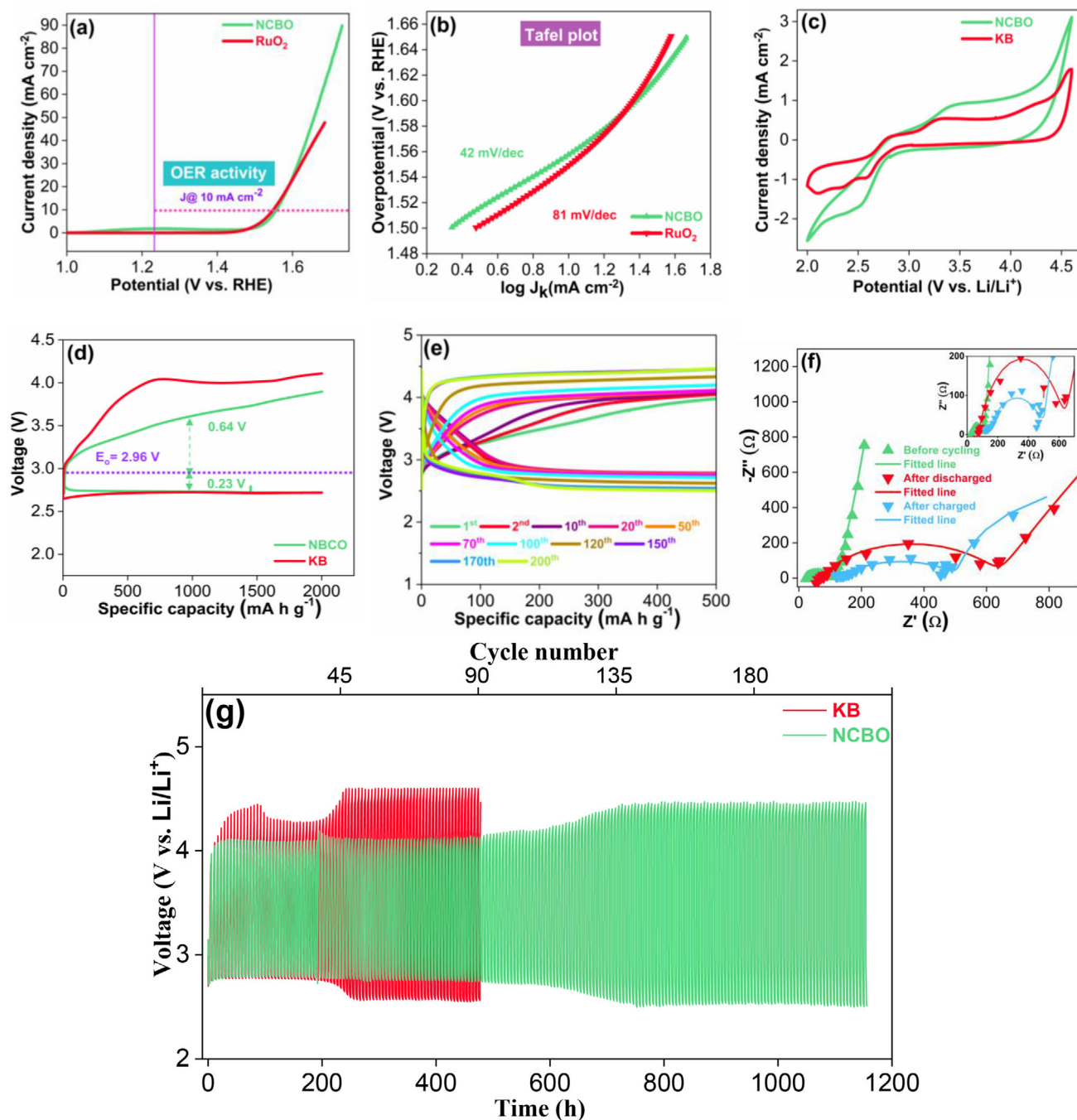


Figure 3. a) iR-corrected LSV plots of OER and b) Tafel plots of the NCBO and RuO₂ catalysts in 1 M KOH electrolyte. c) CV curves of NCBO and KB electrodes at a scan rate of 0.1 mV s⁻¹ and between 2.0 and 4.5 V. d) The discharge/charge profiles of the NCBO and KB electrodes at a current density of 175 mA g⁻¹ and a cut-off capacity of 2000 mA h g⁻¹. e) Cyclic stability test of the NCBO O₂ cathode (current density of 175 mA g⁻¹, cut-off capacity of 500 mA h g⁻¹). f) Nyquist plots (inset: higher magnification of Nyquist plots) and g) long cycle stability test for NCBO and KB electrodes at a current density of 175 mA g⁻¹.

insights into the OER mechanism in the aqueous, alkaline electrolyte system are given following the density functional studies in the next subsection. To probe the long-term OER stability of the NCBO catalyst, a chronopotentiometry (CP) test was performed at a fixed current density. As seen from Figure S2 (Supporting Information), the potential of the NCBO catalyst during the CP

test at current density of 10 mA cm⁻² remains quite stable even after 30 h.

The electrocatalytic activity of the NCBO catalyst was also investigated in a nonaqueous electrolyte. Figure 3c presents the cyclic voltammograms (CV) of NCBO and Ketjen black (KB) at a scan rate of 0.1 mV s⁻¹ between 2.0 and 4.5 V in 1 M lithium

bis(trifluoromethanesulfonimide) (LiTFSi) in tetraethylene glycol dimethyl ether (TEGDME). The cyclic voltammogram of the NCBO cathode electrode shows a cathodic peak at ≈ 2.5 V, which corresponds to the oxygen reduction or discharge reaction (formation of lithium peroxide (Li_2O_2): $\text{O}_2 + 2\text{Li}^+ + 2\text{e}^- \rightarrow \text{Li}_2\text{O}_2$).^[23] The anodic peak at ≈ 3.5 V is ascribed to the oxygen evolution or charge reaction (decomposition of Li_2O_2 : $\text{Li}_2\text{O}_2 \rightarrow \text{O}_2 + 2\text{Li}^+ + 2\text{e}^-$).^[24] The NCBO cathode exhibits an efficient oxygen reduction reaction (ORR) onset potential and higher OER/ORR peak current density than KB, implying that NCBO is more effective in the Li_2O_2 generation/decomposition. This enhanced performance is likely due to the superior electronic conductivity and catalytic activity of NCBO, which facilitate faster electron transfer and more efficient reactions compared to KB.

Figure 3d shows the specific capacity versus voltage profile of the NCBO and KB with a capacity limitation of 2000 mA h g^{-1} at a current density of 175 mA g^{-1} . The NCBO shows a smaller charge overpotential (0.64 V) than KB (1.04 V). This suggests that NCBO catalyzes the decomposition of the discharge products at a lower overpotential, making it more efficient for OER. The cycling stability of the Li- O_2 batteries with the NCBO cathode was evaluated at a current density of 175 mA g^{-1} and at a capacity limitation of 500 mA h g^{-1} (Figure 3e). During the first cycle, the NCBO electrode shows a charge-discharge overpotential of 1.15 V with 70.51% round trip efficiency, after 200 cycles it shows an overpotential of 1.95 V with 56% round trip efficiency.

The charge transfer resistance (R_3) during the discharge and charge process of the NCBO cathode containing Li- O_2 cells was determined using electrochemical impedance spectroscopy (EIS). Figure 3f shows the Nyquist plots of the cell before cycling, after the first discharge, and after the first charge of the NCBO cathode. The EIS data have been simulated by Zsimpwin software using equivalent circuit $R_1(Q_1R_2)(Q_2R_3)W$, where R_1 is solution resistance, R_2 is solid-electrolyte interface resistance, Q_1 and Q_2 are constant phase elements, and W is attributed to the mass transfer of O_2 at the cathode catalyst. The simulated EIS results are given in Table S2 (Supporting Information). The R_3 value of the pristine electrode is $\approx 70 \text{ }\Omega$, which significantly increased to $\approx 559 \text{ }\Omega$ after the discharge, attributable to the accumulation of the insulating Li_2O_2 discharge product on the surface of the electrode. Upon charging, the R_3 value decreases to $\approx 303 \text{ }\Omega$, suggesting the decomposition of Li_2O_2 discharge product on the cathode surface.

The long cyclability of the NCBO cathode was investigated at a capacity limitation of 500 mA h g^{-1} and compared with KB. As shown in Figure 3g, the assembled Li- O_2 cell with the NCBO catalyst shows a smaller charge-discharge voltage gap after 200 cycles and cycled over 1150 h, while for KB increased overpotentials are observed just after 200 h. This is speculated to result from the accumulation of other irreversible discharge products, primarily originating from reactions between the electrolyte, carbon, and lithium at higher charge voltage (>4.5 V), rather than Li_2O_2 , on the cathode surface.

Furthermore, the morphology of transient intermediates formed during the charge/discharge of Li- O_2 batteries was investigated using ex situ Field Emission scanning electron microscope (FE-SEM) analysis. Figure 4a–h presents the FE-SEM images of pristine, discharged, and charged electrodes. The discharged electrode [Figure 4c–f] exhibits the formation of flower-

like $\text{Li}_2\text{O}_2/\text{LiO}_2$ structures on the surface of the NCBO cathode during the fully discharged state. These flower-like $\text{Li}_2\text{O}_2/\text{LiO}_2$ structures completely disappear in the charged state, indicating their decomposition upon charging [Figure 4g,h].

In addition, ex situ XRD (Figure 4i) patterns of pristine, discharged, and charged electrodes were compared with the XRD pattern of commercial Li_2O_2 . In the discharged cathode, the presence of the three diffraction peaks observed at $2\theta = 32.9^\circ$ and 35.0° which correspond to the Li_2O_2 phase in the. The weak intensity of these peaks is attributed to the dominant presence of highly crystalline carbon components (polyvinylidene difluoride (PVDF) and KB) in the sample. Interestingly, these reflections disappeared in the charged cathode, suggesting that the discharge products undergo reversible formation and decomposition during the electrochemical process.^[25] In addition, no distinct diffraction peaks corresponding to LiO_2 were observed in the XRD patterns, likely due to its amorphous nature.^[26]

Similarly, ex situ Raman spectroscopy (Figure 4f) revealed peaks at ≈ 1125 and $\approx 1516 \text{ cm}^{-1}$ in the discharged electrode, indicating the presence of lithium superoxide (LiO_2). The peak at $\approx 1125 \text{ cm}^{-1}$ is characteristic of a LiO_2 -like species, whereas the peak at $\approx 1516 \text{ cm}^{-1}$ is associated with strong interactions between LiO_2 and the graphite carbon surface. Additionally, a low intense peak corresponding to Li_2O_2 was also observed. The relative intensity of LiO_2 was much higher than that of Li_2O_2 , which indicated that LiO_2 was the dominant discharge product. During the charge, the characteristic peaks of LiO_2 and Li_2O_2 were disappeared, indicating their decomposition. Interestingly, catalysts that promote the formation of LiO_2 have been shown to enhance battery performance and cycle life, mainly due to its higher electronic conductivity and lower charge transfer resistance, thereby contributing to a reduced charge overpotential.^[13,15,26–28] The ex situ XPS results of the cycled NCBO cathodes are provided in (Figure S3, Supporting Information).

2.1. Density Functional Theory Calculations

The OER mechanism in the aqueous, alkaline electrolyte system on NCBO was studied by periodic DFT calculations. We considered different surfaces of the NCBO crystal, the structure of which is well described by differently corrected generalized gradient approximation (GGA) functionals (Figure S4 and Table S3, Supporting Information). Surface energies were calculated employing the PBE+U method. The (010) surface (see Figure 5a) is the most stable surface, having a surface energy of $21.4 \text{ meV}\text{\AA}^{-2}$. By cutting normal to the [010] direction, the tetrahedral coordination of the Co atoms is kept intact and only ionic bonds between Na atoms and O atoms of borate molecules are withdrawn. No pronounced relaxation effects occur. To create a (101) surface, not only Na–O bonds but also Co–O bonds need to be broken, leading to threefold coordinated surface Co atoms (see Figure 5b). If no ionic relaxation were allowed, this would be associated with an energy penalty of $53.3 \text{ meV}\text{\AA}^{-2}$. However, due to a rearrangement of the threefold coordinated surface Co atoms toward neighboring tetrahedral sites, a considerable energy gain is obtained. The resulting surface structure contains units of two corner sharing, distorted CoO_4 -tetrahedrons and has a surface energy of $31.9 \text{ meV}\text{\AA}^{-2}$. Other surfaces, such as the (001) and (011) surfaces,

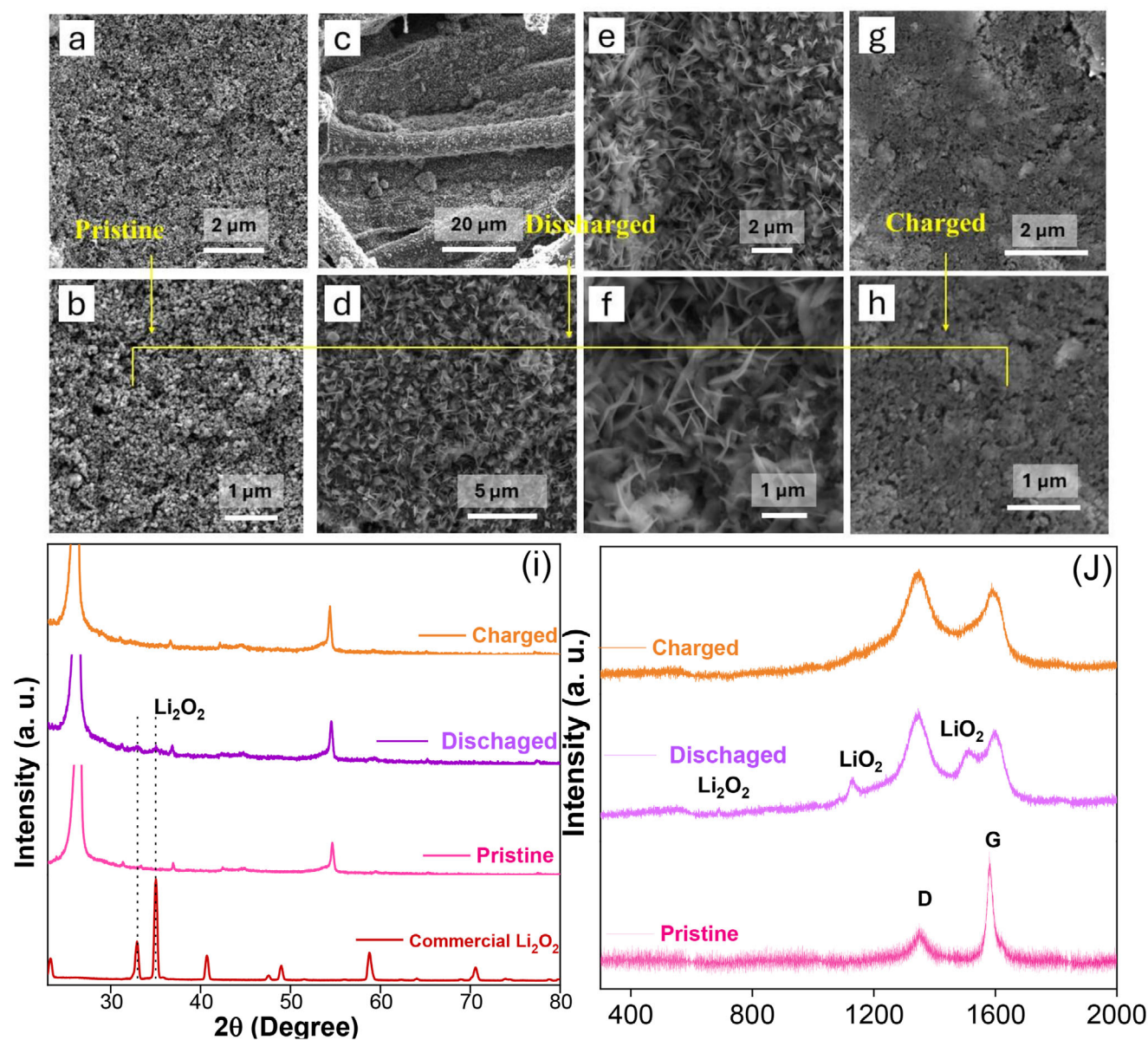
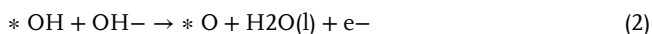


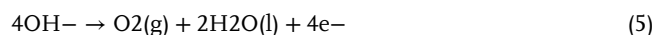
Figure 4. Ex situ analysis of the NCBO cathode: FESEM images of a,b) pristine, c–f) discharged and g,h) charged electrodes; i) XRD patterns; and j) Raman spectra of the pristine, discharged, and charged electrodes.

have higher surface energies (75.4 and 39.3 meV Å^{−2}, respectively) and were not considered in the calculations of the OER mechanism.

Our calculations of the OER mechanism are based on the commonly employed assumption that the alkaline OER proceeds in four elementary steps, where * indicates the adsorption of intermediates onto the catalyst surface:



leading to the total reaction as follows.



We would like to note that the electronic structure of NCBO strongly depends on the strength of the on-site correction for highly correlated electrons (Figure S5, Supporting Information), unlike the geometrical structure that depends merely on the actual value of the Hubbard correction (Table S3, Supporting Information). This may impact the interaction of different adsorbates with the substrate to different degrees. Therefore, the OER mechanism has been studied by employing different values for

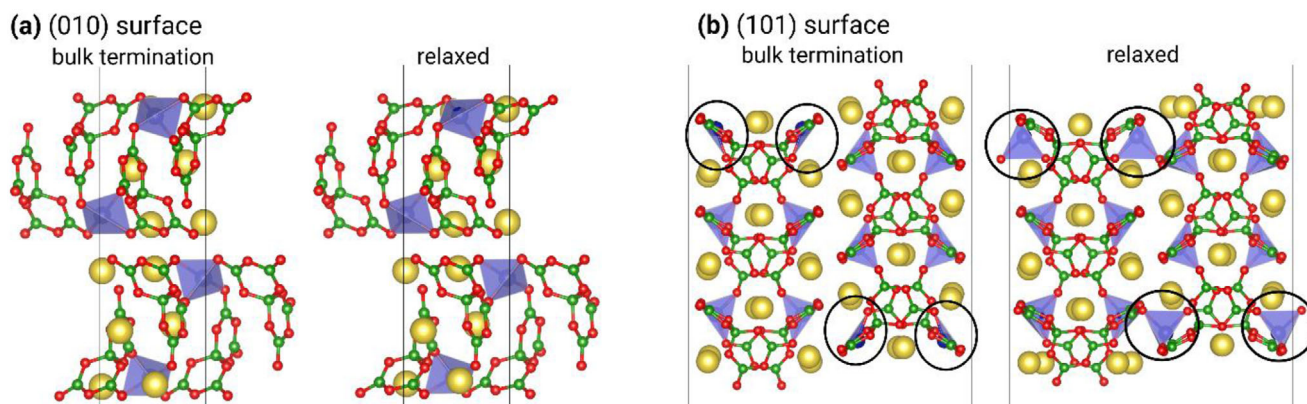


Figure 5. a) The (010) surface and b) the (101) surface slabs of NCBO before (left) and after (right) ionic relaxation (Color coding correlates to the image in Figure 1(b)). In (b) black circles mark the strong relaxation of the threefold coordinated Co surface atoms leading to a tetrahedral coordination.

the Hubbard correction. Further details on the calculations of the individual reaction energies and the overpotential are given in the [Supporting Information](#), page 26–27.

The reaction energies and structures of the intermediates of the OER at the (010) surface of NCBO is shown in [Figure 6a,c](#), respectively. The first reaction step involves the adsorption of OH. This leads to a change of the fourfold tetrahedral coordination of Co to a distorted fivefold bipyramidal coordination. The charge of Co, as calculated according to a Bader charge analysis, increases from +1.27 e for the bare surface to +1.59 e for the OH adsorption complex. This reflects the increase in the oxidation state of Co. Besides the bonding of OH to Co, Na surface atoms stabilize the OH adsorption. If the PBE+U method is used, the Na–O distances of the adsorption complex are 2.35 and 2.39 Å, which are close to the Na–O distances reported for NaOH (2.29, 2.37, and 2.40 Å for space group P21/m^[29] as well as 2.31 and 2.38 Å for space group Cmc21^[30]).

The following reaction from adsorbed OH to an adsorbed O atom (reaction step 2) is associated with the highest step in energy and thus represents the potential determining step (PDS). The Co–O distance clearly decreases from 1.99 to 1.64 Å, the charge on Co slightly diminishes to +1.50 e. The charge on Co remains at $\approx +1.49$ e after the formation of adsorbed OOH (reaction step 3). The adsorption complex of OOH includes less distorted bipyramidal coordination of Co, with a Co–O distance of 1.97 Å. Finally, the release of O₂ (reaction step 4) is an exergonic process at pH 13.

Applying a “+U” correction of 3.5 eV to the pure or dispersion-corrected GGA functionals, the structures of the intermediates of the alkaline OER mechanism as well as their thermodynamic energies are rather similar for the PBE and the RPBE-D3 functional. The overpotential is 0.76 eV for the PBE+U(3.5 eV) method and 0.74 eV for RPBE-D3 + U(3.5 eV). At a lower coverage (0.25 molecules per surface unit cell, not shown), the overpotential decreases slightly to 0.74 V if the PBE + U(3.5 eV) method is applied.

Yet, a remarkable decrease in the individual reaction energies ΔG_i is obtained if a smaller “+U”-parameter of 2.5 eV is employed, leading to an overpotential of 0.55 V.

The impact of the electronic correlation on the overpotential of the OER was already observed by García-Mota et al., who also

found a destabilization of the O, OH, and OOH adsorbates on Co-oxide and -oxyhydroxide surfaces due to the Hubbard correction, which is most pronounced for the adsorbed O-atom.^[31] According to their RPBE+U(U = 3.5 eV) calculations, the overpotential of the OER is 0.76 V at a Co₃O₄ surface and 0.78 V at a CoOOH surface, which is ≈ 0.35 V (Co₃O₄ surface) or 0.51 V (CoOOH surface) larger than the overpotential calculated with the uncorrected GGA functional RPBE.^[32] Notably, though different coordination environments of Co are present, the overpotentials calculated at the Co-oxide surfaces are close to our calculated overpotentials at the (010) surface, if comparable methods are used. Additionally, the impact of explicit solvent molecules on the OER was studied by employing static models of the (010) surface that include one or six water molecules per unit cell (Figure S6, Supporting Information). As previously, the second reaction step (*OH → *O) represents the PDS. Yet, as the adsorption of OH is energetically less favorable in the presence of water molecules, the overpotential, calculated by the PBE+U method, decreases to 0.61 eV (for one co-adsorbed H₂O per surface unit cell) or 0.63 eV (for 6 co-adsorbed H₂O molecules per surface unit cell).

We observe an exergonic adsorption of OH, for the slightly less stable (101) surface of NCBO. The free energy of reaction step (1) at the bare surface is ≈ -0.5 eV. This energy gain can be explained by the fact that upon OH adsorption, the surface relaxation effect, which leads to Co atoms coordinated within two corner-sharing tetrahedrons, is relieved. Instead, the original tetrahedral coordination of Co atoms in bulk is restored by replacing the missing borate-oxygen at the surface with OH (see purple OH in Figure 5d). Thus, at pH 13, the (101) surface is at least partially covered with OH, and to study the OER reaction mechanism at the (101) surface, co-adsorbed OH molecules need to be taken into account. The results of different calculations of the OER mechanism at such a surface are shown in Figure 6b,d. The adsorption of the second OH molecule occurs at the second surface Co atom of the unit cell, leading to a tetrahedrally coordinated Co atom at the surface in the same fashion as already observed for the adsorption of the first OH. At the second reaction step, leading to the formation of an adsorbed O-atom, the tetrahedral coordination gets distorted: the adsorbed O atom is slightly displaced toward the surface Na atoms. The Na–O

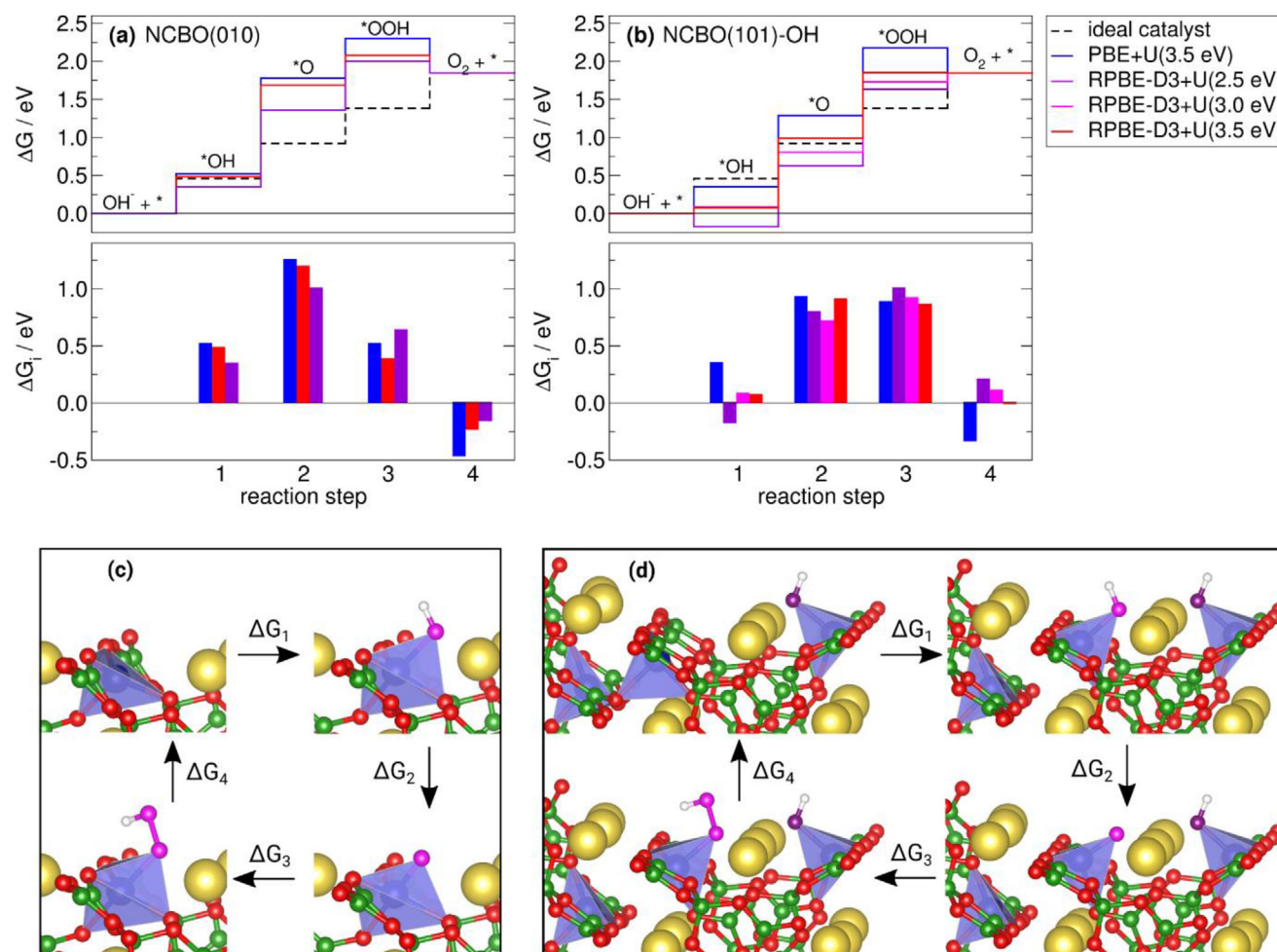


Figure 6. a,b) Total reaction energies $\Delta G(j) = \sum_i \Delta G_i$ (upper panels) and individual reaction energies ΔG_i (lower panels) for the alkaline OER reaction steps (pH 13) calculated (a) at the bare (010) and (b) at the partially OH-covered (101) surface of NCBO with different exchange correlation functionals and different values of the Hubbard-like correction term U. The structural models of the individual reaction steps at the (010) and partially OH-covered (101) surface are shown in subfigures c,d), respectively. The color-coding of most of the atoms is given in Figure 1b, pink atoms reflect oxygen atoms involved in the OER, purple atoms denote the oxygen of the pre-adsorbed OH molecule, and white atoms are hydrogen.

distances are 2.31 and 2.33 Å, suggesting that there are electrostatic Na–O interactions that stabilize the adsorbed O atom. The reaction energy of this step is much lower than the corresponding value at the (010) surface. Furthermore, it is comparable to the energy of the formation of adsorbed OOH for which the tetrahedral coordination is restored.

According to PBE+U calculations, the overpotential is associated with reaction step 2 as PDS and amounts to 0.47 V, which is 0.29 V lower than the overpotential at the (010) surface. If the RPBE-D3+U method is used, the overpotential amounts to 0.45, 0.46, or 0.54 V for $U = 3.5, 3.0$, or 2.5 eV, respectively. For $U \leq 3.0$ eV the PDS changes from reaction step 2 to reaction step 3.

Noteworthy and possibly also assignable to other GGA + U calculations of the OER at inorganic surfaces, is the fact that the nature of the PDS and the actual value of the overpotential both depend on the strength of the Hubbard correction applied on top of the GGA functional in order to cope with the strongly correlated d-electrons of Co.

3. Conclusion

A tetrahedrally coordinated cobalt borate (NCBO) material has been explored as an OER catalyst for rechargeable Li–O₂ battery applications. The catalyst displayed an efficient OER performance in 1 M KOH solution with an OER overpotential of 326 mV_{RHE} at a current density of 10 mA cm^{−2} and a small Tafel slope of 42 mV dec^{−1}. DFT calculations revealed a preferred OER at the OH-covered (101) surface of NCBO with an overpotential in the range of ≈451–544 mV. The calculated overpotential is slightly larger than the measured one, however, regarding the simplifications and assumptions of the calculational setup, the computational values compare reasonably well to the experimentally determined value. The reaction steps in which the adsorbed O or OOH are formed might be both the PDS as they have almost equal reaction energies. A rechargeable Li–O₂ battery was constructed using NCBO as an air cathode. The NCBO catalyst shows a smaller charge overpotential of 0.64 V at a capacity limitation

of 2000 mA h g⁻¹ and a current density of 175 mA g⁻¹. The long-cycle stability of the NCBO cathode was evaluated at a limited capacity of 500 mA h g⁻¹ for 200 cycles, delivering an overpotential of 1.95 V and a 56.00% round-trip efficiency. Post-mortem analysis of cycled NCBO electrodes revealed electronically conductive Lithium Superoxide as the dominant discharge product.

4. Experimental Section

Materials: The chemicals used for the NCBO synthesis were Na₂CO₃ (Merck India, 99.5%), (Co(OH)₂, (Sigma–Aldrich, 95%), and H₃BO₃ (Merck India, 99.5%).

For electrochemical activity tests, the following chemicals and materials were used: Potassium hydroxide (KOH, AR, 99%, SRL, India), Nafion ionomer (Sigma–Aldrich), ethanol (Merck India), Milli-Q water, and The catalyst RuO₂ (99.9% trace metals basis, Sigma–Aldrich) was purchased for comparative studies.

For Li–O₂ battery studies, the following chemicals and materials were utilized: The following chemicals and materials used for Li–O₂ battery studies lithium disc (8 mm diameter, Alfa–Aesar), glass microfiber separator (Whatman, Sigma–Aldrich), KB, (akzonobel), PVDF, (Sigma–Aldrich), N-methyl-2-pyrrolidone (NMP, Sigma–Aldrich), carbon paper (SIGRACET GDL 38 BC), TEGDME, (Sigma–Aldrich) and highly pure oxygen (99.999% purity, INDO GAS).

Material Synthesis: NCBO was prepared by a conventional ceramic method. All chemicals were dried in a vacuum oven at 70 °C for 24 h before use. Stoichiometric amounts of Na₂CO₃, Co(OH)₂, and H₃BO₃ were ball milled for 40 min under argon using a high-energy milling apparatus (Fritsch P-23). The obtained solid was hand-ground and heated to 700 °C for 1 h in a tube furnace (Ants Ceramics, India) under argon flow. The prepared sample was stored in an Ar-filled glovebox until use to avoid oxidation by moist air.

Material Characterization: XRD patterns of the prepared borate were measured on a Bruker D8 Advance Da Vinci diffractometer using Cu Kα (λ = 1.5418 Å) radiation. The oxidation state of the samples was determined from XPS using a Thermo Fischer K-Alpha™ Spectrometer with non-monochromatic Al Kα radiation (1486.7 eV). The C 1s peak of the adventitious carbon (284.8 eV) was used as the reference binding energy for calibration. The morphological features were observed on a Carl Zeiss 130 VP FESEM.

Raman spectra were taken on an TechnoS IndirAM CTR 500C Micro Raman Spectrometer using a 532 nm diode laser. High-resolution transmission electron microscopy (HRTEM) images were obtained with a Thermo Scientific Talos F200S. The elemental mapping of the NCBO was obtained by Bruker EDX attached to HRTEM.

Electrochemical Activity Tests: Rotating-disc electrode experiments were carried out in a PINE RDE setup with glassy carbon (5 mm in diameter, PINE Research Instrumentation, Inc. USA) as the working electrode, Pt wire as the counter electrode and Hg/HgO (1 M KOH) as the reference electrode. The catalyst ink was prepared by mixing 14 mg of catalyst and 4 mg carbon black in a mixture of 100 μL of Nafion ionomer, 600 μL of ethanol and 300 μL Milli-Q water. The 10 μL dispersed catalyst ink was cast on the glassy carbon (loading = 0.7 mg cm⁻²). The catalytic activity (OER) studies of the catalysts were carried out in both N₂ and O₂-saturated aqueous 1 M KOH electrolyte solutions.

The potentials recorded and referred to Hg/HgO in each experiment were calculated using the formula

$$\text{ERHE} = \text{EHg/HgO} + 0.059 \text{ pH} + 0.198 \text{ V} \quad (6)$$

where E_{Reversible hydrogen electrode (RHE)} is the potential versus RHE, E_{Hg/HgO} is the potential versus Hg/HgO electrode, and 1 M KOH accounts for a pH of 13.

The RuO₂ catalyst with the same loading was prepared using the same method for comparison.

Li–O₂ Battery Fabrication and Testing: The Li–O₂ battery studies of prepared catalysts were carried out in a Swagelok-type cell in an argon-filled glovebox. A lithium disc (8 mm) was used as the anode with a glass microfiber separator. The cathode disc was prepared by depositing the slurry mixture of catalyst, KB, and PVDF in NMP on the carbon paper, with a catalyst: KB: PVDF ratio of 60:40:10). A 10 mm diameter coated gas diffusion layer (GDL) with a catalyst loading of ≈0.3–0.5 mg cm⁻² was used as the cathode in the Li–O₂ cell. The current density and specific capacity of the cathode were calculated based on the mass of the cathode catalyst. The specific capacity and current density were expressed in terms of the total mass of the cathode catalyst. 1 M LiTFSi in TEGDME was used as the electrolyte. Highly pure oxygen at a pressure of 1 bar was supplied from the direction of the cathode for cell reactions. The galvanostatic charge–discharge, cyclic voltammetry, and electrochemical impedance spectroscopy (EIS) studies were conducted at room temperature using VMP3Z biologic multi-channel. For the EIS analysis, a frequency range of 10 mHz–1 MHz with an amplitude of 10 mV was used.

Computational Method: The Vienna ab initio simulation package (VASP 5.4) is used [33,34] to perform periodic density functional theory calculations. The electron-ion interaction was described by the projected augmented wave method.[35,36] The electronic wave functions were expanded in a plane wave basis set up to a cutoff energy of 500 eV. The generalized gradient approximation (GGA) was employed to calculate the exchange and correlation energy. In detail, mainly the PBE functional[37] was used. For comparison, its revised version of Hammer and Nørskov (RPBE)[38] in combination with the semi-empirical correction scheme for dispersive interactions of Grimme (D3)[39] was consulted. The damping function proposed by Chai and Head-Gordon (“zero-damping”) was chosen to circumvent the divergence of the dispersion correction at short distances.[40] To account for on-site Coulomb interactions a Hubbard like term (+U) was added in the way proposed by Dudarev.[41] When the PBE or RPBE functional were used without dispersion correction, the values of U_{eff} = U–J were set to U = 3.5 eV and J = 0 eV for the Co-atoms in NCBO, following the suggestions given for PBE[42] and for RPBE.[31] In case of the dispersion corrected RPBE functional, a slightly different value of the Hubbard parameter was additionally employed (U = 2.5 eV), as previously determined.[43]

All geometry optimizations were carried out until all forces on atoms were less than 0.01 eV Å⁻¹. The electronic structure was converged within 10⁻⁶ eV. For the integration over the first Brillouin zone, a Gaussian smearing of 0.05 eV was used. Furthermore, calculations of bulk NCBO employed a 7 × 1 × 5 k-point mesh.

The NCBO surfaces were modeled by symmetric slabs consisting of formula units that were separated by a vacuum region of 15 Å. During geometry optimization, the atoms in the middle of the (101) slab and the atoms in the lower half of the (010) slab were kept fixed to mimic the bulk structure. For calculations of the (010) and (101) surface a 7 × 1 × 5 and a 5 × 1 × 1 k-point mesh was employed, respectively.

Supporting Information

Supporting Information is available from the Wiley Online Library or from the author.

Acknowledgements

The authors gratefully acknowledge the Department of Science & Technology (DST), New Delhi, India for their financial support (Grant No.DST/CEST/AMEST/2022/65(G)) and thank the CSIR-CECRI for providing access to the characterization (CIF) facilities. CSIR-CECRI manuscript number: CECRI/PESVC/Pubs./2024-172. The authors gratefully acknowledge computer time provided by the state of Baden-Württemberg through bwHPC and the DFG through grant no. INST 40/575-1 FUGG (JUSTUS 2 cluster). The work contributes to the research performed at CELEST (Center for Electrochemical Energy Storage Ulm-Karlsruhe).

Open access funding enabled and organized by Projekt DEAL.

Conflict of Interest

The authors declare no conflict of interest.

Data Availability Statement

The data that support the findings of this study are available from the corresponding author upon reasonable request.

Keywords

density functional theory, Li-O₂ battery, oxygen evolution reaction, sodium cobalt borate

Received: February 18, 2025

Revised: May 2, 2025

Published online:

- [1] H.-D. Lim, B. Lee, Y. Bae, H. Park, Y. Ko, H. Kim, J. Kim, K. Kang, *Chem. Soc. Rev.* **2017**, 46, 2873.
- [2] S. Guo, L. Zou, M. Sun, Z. Wang, S. Han, B. Chi, J. Pu, J. Li, *ACS Appl. Energy Mater.* **2020**, 3, 10015.
- [3] G. Liu, H. Chen, L. Xia, S. Wang, L.-X. Ding, D. Li, K. Xiao, S. Dai, H. Wang, *ACS Appl. Mater. Interfaces* **2015**, 7, 22478.
- [4] J. Wang, X. Cheng, Z. Li, M. Xu, Y. Lu, S. Liu, Y. Zhang, C. Sun, *ACS Appl. Energy Mater.* **2018**, 1, 5557.
- [5] K. R. Yoon, K. Shin, J. Park, S.-H. Cho, C. Kim, J.-W. Jung, J. Y. Cheong, H. R. Byon, H. M. Lee, I.-D. Kim, *ACS Nano* **2018**, 12, 128.
- [6] Y. Li, J. Lu, *ACS Energy Lett.* **2017**, 2, 1370.
- [7] F. Strauss, G. Rousse, M. T. Sougrati, D. A. Dalla Corte, M. Courty, R. Dominko, J.-M. Tarascon, *Inorg. Chem.* **2016**, 55, 12775.
- [8] P. Barpanda, L. Lander, S. i. Nishimura, A. Yamada, *Adv. Energy Mater.* **2018**, 8, 1703055.
- [9] H. Kim, J. Park, I. Park, K. Jin, S. E. Jerng, S. H. Kim, K. T. Nam, K. Kang, *Nat. Commun.* **2015**, 6, 1.
- [10] A. Baby, D. Singh, C. Murugesan, P. Barpanda, *Chem. Commun.* **2020**, 56, 8400.
- [11] L. Sharma, R. Gond, B. Senthikumar, A. Roy, P. Barpanda, *ACS Catal.* **2019**, 10, 43.
- [12] D. Dwibedi, R. Gond, P. Barpanda, *Chem. Mater.* **2019**, 31, 7501.
- [13] H.-H. Wang, C. Zhang, J. Gao, K. C. Lau, S. T. Plunkett, M. Park, R. Amine, L. A. Curtiss, *Faraday Discuss.* **2024**, 248, 48.
- [14] P. Seraji, H. Shahbazi, M. K. Ncube, N. Shan, F. Lagunas, I. Papailias, P. Navabi, C. Zhang, A. Jaradat, S. Kadkhodaei, *Nano Energy* **2025**, 134, 110510.
- [15] C. Zhang, S. Wang, T. Yang, N. Shan, S. K. Singh, A. Jaradat, M. K. Ncube, P. Redfern, A. Subramanian, Z. Huang, *Energy Storage Mater.* **2023**, 60, 102844.
- [16] J. Lu, Y. Jung Lee, X. Luo, K. C. Lau, M. Asadi, H.-H. Wang, S. Brombosz, J. Wen, D. Zhai, Z. Chen, *Nature* **2016**, 529, 377.
- [17] S. T. Plunkett, A. Kondori, D. Y. Chung, J. Wen, M. Wolfman, S. H. Lapidus, Y. Ren, R. Amine, K. Amine, A. U. Mane, *ACS Energy Lett.* **2022**, 7, 2619.
- [18] S. T. Plunkett, C. Zhang, K. C. Lau, M. R. Kephart, J. Wen, D. Y. Chung, D. Phelan, Y. Ren, K. Amine, S. Al-Hallaj, *Nano Energy* **2021**, 90, 106549.
- [19] A. Halder, H.-H. Wang, K. C. Lau, R. S. Assary, J. Lu, S. Vajda, K. Amine, L. A. Curtiss, *ACS Energy Lett.* **2018**, 3, 1105.
- [20] A. Halder, A. T. Ngo, X. Luo, H.-H. Wang, J. Wen, P. Abbasi, M. Asadi, C. Zhang, D. Miller, D. Zhang, *J. Phys. Chem. A* **2019**, 123, 10047.
- [21] J. Masa, P. Weide, D. Peeters, I. Sinev, W. Xia, Z. Sun, C. Somsen, M. Muhler, W. Schuhmann, *Adv. Energy Mater.* **2016**, 6, 1502313.
- [22] X. Cao, L. Cui, X. Wang, W. Yang, J. Liu, *ChemCatChem* **2018**, 10, 2826.
- [23] Z. Wang, X. Peng, S. Guo, M. Sun, J. Cheng, L. Zou, B. Chi, J. Pu, *ACS Appl. Energy Mater.* **2021**, 4, 9376.
- [24] Q. Xia, L. Zhao, D. Li, J. Wang, L. Liu, C. Hou, X. Liu, H. Xu, F. Dang, J. Zhang, *J. Mater. Chem. A* **2021**, 9, 19922.
- [25] S. Guddehalli Chandrappa, G. Karkera, V. A. Gangadharappa, D. Chen, R. A. Caruso, P. S. Annigere, *ACS Appl. Energy Mater.* **2022**, 5, 14680.
- [26] Y. S. Jeong, J.-B. Park, H.-G. Jung, J. Kim, X. Luo, J. Lu, L. Curtiss, K. Amine, Y.-K. Sun, B. Scrosati, *Nano Lett.* **2015**, 15, 4261.
- [27] D. Zhai, H.-H. Wang, J. Yang, K. C. Lau, K. Li, K. Amine, L. A. Curtiss, *J. Am. Chem. Soc.* **2013**, 135, 15364.
- [28] M. W. Yuan, C. Y. Nan, Y. Yang, G. B. Sun, H. F. Li, S. L. Ma, *ACS Omega* **2017**, 2, 4269.
- [29] H.-J. Bleif, H. Dachs, *Acta Cryst. A* **1982**, 38, 470.
- [30] H. Stehr, *Z. für Kristallogr. Cryst. Mater.* **1967**, 125, 332.
- [31] M. García-Mota, M. Bajdich, V. Viswanathan, A. Vojvodic, A. T. Bell, J. K. Nørskov, *J. Phys. Chem. C* **2012**, 116, 21077.
- [32] M. Bajdich, M. García-Mota, A. Vojvodic, J. K. Nørskov, A. T. Bell, *J. Am. Chem. Soc.* **2013**, 135, 13521.
- [33] G. Kresse, J. Furthmüller, *Phys. Rev. B* **1996**, 54, 11169.
- [34] G. Kresse, J. Furthmüller, *Comput. Mater. Sci.* **1996**, 6, 15.
- [35] P. E. Blöchl, *Phys. Rev. B* **1994**, 50, 17953.
- [36] G. Kresse, D. Joubert, *Phys. Rev. B* **1999**, 59, 1758.
- [37] J. P. Perdew, K. Burke, M. Ernzerhof, *Phys. Rev. Lett.* **1996**, 77, 3865.
- [38] B. Hammer, L. B. Hansen, J. K. Nørskov, *Phys. Rev. B* **1999**, 59, 7413.
- [39] S. Grimme, J. Antony, S. Ehrlich, H. Krieg, *J. Chem. Phys.* **2010**, 132, 154104.
- [40] J.-D. Chai, M. Head-Gordon, *Phys. Chem. Chem. Phys.* **2008**, 10, 6615.
- [41] S. L. Dudarev, G. A. Botton, S. Y. Savrasov, C. Humphreys, A. P. Sutton, *Phys. Rev. B* **1998**, 57, 1505.
- [42] L. Wang, T. Maxisch, G. Ceder, *Phys. Rev. B Condens. Matter Mater. Phys.* **2006**, 73, 195107.
- [43] K. Forster-Tonigold, J. Kim, J. Bansmann, A. Groß, F. Buchner, *ChemPhysChem* **2021**, 22, 441.